Acta Materialia 208 (2021) 116694

Contents lists available at ScienceDirect

Acta Materialia

journal homepage: www.elsevier.com/locate/actamat

Subsurface structural change of silica upon nanoscale physical contact: Chemical plasticity beyond topographic elasticity

Hongtu He[a,b,*], Zhe Chen[b], Yen-Ting Lin[b], Seung Ho Hahn[c], Jiaxin Yu[a], Adri C.T. van Duin[c], Tobias D. Gokus[d], Slava V. Rotkin[e], Seong H. Kim[b,*]

[a] Key Laboratory of Testing Technology for Manufacturing Process, Ministry of Education, Southwest University of Science and Technology, Mianyang, Sichuan 621010, China
[b] Department of Chemical Engineering and Materials Research Institute, Pennsylvania State University, PA 16802, USA
[c] Department of Mechanical Engineering, Pennsylvania State University, PA 16802, USA
[d] neaspec GmbH, Eglfinger Weg 2, Haar, Munich D-85540, Germany
[e] Materials Research Institute and Department of Engineering Science & Mechanics, Pennsylvania State University, University Park, PA, USA

ARTICLE INFO

Article history:
Received 13 October 2020
Revised 12 January 2021
Accepted 24 January 2021
Available online 10 February 2021

Keywords:
Silica glass
Nanoscratch
Nanoindentation
Subsurface damage
Bond length distribution

ABSTRACT

Surface defects or flaws on materials made by physical contacts with foreign objects can deteriorate their mechanical properties and limit technical applications. Thus, understanding the contact-induced subsurface damage is of great importance. Using nanoscale infrared spectroscopy and reactive molecular dynamics simulations, the subsurface structural changes of silica upon nanoindentation and nanoscratch are investigated. The results reveal an elongation of the Si–O bond length distribution even after the topographically-elastic contact, indicating a "chemical plasticity" at the sub-Angstrom level. In the plastic region with subsurface densification, the Si–O bond is found to be slightly longer than the pristine region, indicating the decrease in molar volume is accompanied with the elongation, not shortening, of the Si–O bond. These results elucidate the structural damage of a material upon physical contact cannot be delineated based on the topographic deformation of the surface.

1. Introduction

Due to intrinsic chemical and mechanical stabilities as well as optical transparency, oxide glasses are widely used for optical fibers, optoelectronics, display panels, solar modules, and so on [1–4]. Once manufactured into functional shapes, they are subject to physical contacts with foreign materials during storage, transport, installation, and in-service. Such contacts will introduce extrinsic defects to the surface [5,6]. Even if physical contacts are made far below the indentation or shear damage threshold, thus leaving no topographic damage, such "mild" contacts can still make invisible chemical defects to the glass [7–10]. Those invisible surface defects can deteriorate the mechanical strength or chemical durability of the material [11–13]. Then, the in-service performance is not governed by the intrinsic properties anymore; it will be the extrinsically-introduced surface defects that determine optical properties and mechanical strengths. Thus, it is of paramount importance to understand what structural changes are made in the glass network by the physical contact with foreign objects.

Various short- and medium-range structural aspects of amorphous glass networks can be analyzed with x-ray scattering, nuclear magnetic resonance, and vibrational spectroscopy [14–17]; but, they do not have sufficient spatial resolution or detection sensitivity to analyze glass structures at or around surface defects that are often highly localized or heterogenous [18–20]. In this study, we use nanoscale-infrared spectroscopy (nano-IR) based on scattering-type scanning near-field optical microscopy (s-SNOM) which can provide a spatial resolution of 20-30 nm in the surface plane and 30–50 nm in the depth direction [21–23], to analyze structural changes in the glass network upon nanoindentation and nanoscratch. A silica glass was chosen for comparison with extensive literatures on its nanoindentation and nanoscratch properties [24,25]. Although compositionally simple, the silica glass network can have complicated structural responses, through combinations of changes in Si–O bond length distribution as well as O–Si–O and Si–O–Si bond angle distributions, to accommodate strains induced by externally applied mechanical stress [26–36]. By combining with the recent advancement in spectral interpretation of the Si–O stretching mode of silica [37,38] and reactive molecular dynamics (MD) simulations, we find that the Si–O bond length of the glass network is elongated even in the elastic contact region

* Corresponding authors:
E-mail addresses: hehongtu@swust.edu.cn (H. He), shk10@psu.edu (S.H. Kim).

https://doi.org/10.1016/j.actamat.2021.116694
1359-6454/

as well as in the subsurface region where local molar volume is decreased due to indentation.

2. Materials and methods

2.1. Nanoscratch and nanoindentation

Fused quartz plates (Technical Glass Products Inc., Painesville, OH) with a thickness of 1 mm were used as a silica glass substrate. More details about the sample and the cleaning procedure can be found elsewhere [7–9]. The root-mean-square (RMS) roughness over a 2 × 2 μm^2 area was found to be 0.3 nm, which was negligible compared to the tip penetration depth during the mechanical testing. The nanoindentation and nanoscratch tests were performed with a Hysitron Triboindenter TI-980 (Minneapolis, MN) at room temperature (~22 °C) in air with a relative humidity of 40%. A Berkovich diamond tip and a cono-spherical diamond tip with an effective radius ~150 nm were used for nanoindentation and nanoscratch tests, respectively. The nanoindentation tests were conducted with a maximum load of 5 mN, and the loading-holding-unloading time was set to 5s-2s-5s. The nanoscratch tests were carried out in constant-load and ramp-load scratch modes. The constant load scratch was performed at an applied load of 3 mN and 7 mN with a scratch speed of 1 μm/s. The ramp load scratch was performed while increasing the load at a constant rate from 0 mN to 3 mN with a scratch speed of 1 μm/s. The sliding distances in all nanoscratch tests were set to 10 μm. The sub-T_g annealing temperature was 1000 °C.

2.2. IR spectroscopy with scattering-type scanning near-field optical microscopy (s-SNOM)

The nanoscale IR spectroscopy analysis was performed using a custom-made neaSNOM microscope (-neaspec GmbH) equipped with atomic force microscopy (AFM), and combined UV-Vis-NIR-MIR system of pulsed and continuous-wave (CW) laser sources. For Fourier transform IR spectroscopy, tunable, broadband mid-infrared supercontinuum laser pulses (ca. 680–1500 cm^{-1}) generated by a difference frequency generation laser source (FemtoFiber dichro mid-IR, Toptica) were focused onto a metal coated AFM tip (nano-IR tips, neaspec) passing a beam splitter which was part of an asymmetric Michelson interferometer (nano-FTIR module, neaspec), where the sample and tip were each positioned in one arm of the interferometer. The tip-scattered light was collected by a high-NA parabolic mirror objective and guided together with the reference beam on a liquid nitrogen-cooled mercury cadmium telluride (MCT) detector. Interferograms of the tip-scattered light were obtained by translation of the mirror in the reference arm and recording the detector signal as position of the mirror displacement. Subsequent Fourier transform of the interferograms yielded simultaneously near-field amplitude and phase spectra of the tip scattered fields.

In order to obtain background-free nano-FTIR spectra, the AFM of the s-SNOM setup was operated in intermittent contact mode, where the AFM tip was oscillating vertically (~50 nm) with a frequency Ω close to the mechanical resonance frequency of the cantilever. For separating the near-field signal from spurious far-field signal contributions, demodulation of the detector signal at a higher harmonics n of Ω (n>1) was used. Each sample spectrum was normalized to a reference spectrum measured on a clean silicon sample surface, yielding normalized near-field amplitude and phase spectra, S_n/S_n (Si) and φ_n - φ_n (Si), respectively. Near-field amplitude and phase spectra with demodulation order $n = 2$ are plotted. The data were recorded with a spectral resolution of 8 cm^{-1}.

For s-SNOM imaging, an 8-chip set of mid-IR tunable quantum cascade lasers (Daylight Solutions) generated MIR CW illumination with wavenumbers ranging from 800 cm^{-1} and 1400 cm^{-1}. The back-scattered IR amplitude (S_n) and phase (φ_n) signals were recorded in a pseudo-heterodyne detection mode at the second harmonic ($n = 2$) of the tapping frequency of the AFM probe to extract the near-field signal without background interference. Pt-coated Si AFM tips with an apex radius of ~25 nm (Arrow NCPt, Nanoworld) were used and operated with a tapping amplitude of ~50 nm. The scanned area was 2 μm × 2 μm for the nanoindentation mark, 3 μm × 1 μm for the constant-load nanoscratch track, and 12 μm × 3 μm for the ramp-load nanoscratch track. A schematic illustration showing the s-SNOM measurement of a nanoscratch is presented in Fig. 1a. During scanning, the AFM topography and corresponding s-SNOM signals were obtained simultaneously.

2.3. ReaxFF MD simulations

Molecular dynamics (MD) simulations were carried out with ReaxFF potentials to investigate the subsurface structural changes after nanoscratch at the atomic level. We modeled an amorphous silica (5184 atoms) as a substrate material and the diamond indenter (3515 atoms) with a spherical shape (radius = 1.5 nm) as a counter-surface. Further details of the model construction process are elaborated in the Supporting Information. To mimic humid air condition during the nanoscratch experiments, 150 H_2O molecules were introduced in the space between the substrate and the indenter during the MD simulation. The initial configuration was first equilibrated under canonical ensemble (NVT - constant number of atoms, system volume, and temperature) at 300 K for 100 ps. Then, the indenter was engaged to the substrate and moved across in the x-direction for the nanoscratch simulation. The contact pressure, sliding speed, and sliding distance were 10 GPa, 10 m/s, and 4 nm, respectively. After the nanoscratch process, the substrate was extracted and equilibrated for 50 ps before analyzing glass network structure parameters (Si–O bond length and Si–O–Si bond angle). This represents the structural data immediately after the nanoscratch test. Following the equilibration step, the system temperature was increased to investigate the effect of annealing to the scratched substrate material. The substrate was subject to gradual increase (10 K/ps) of temperature from 300 K to 1500 K and was maintained for 1 ns. The system was cooled back to 300 K at a rate of 5 K/ps and structural information was obtained from the 50 ps-run of equilibration at 300 K. ReaxFF-MD simulations in canonical ensemble (NVT, Nosé-Hoover thermostat with τ = 100 fs) were carried out with ReaxFF implementation in Large-scale Atomic/Molecular Massively Parallel Simulator (LAMMPS) package [39]. Integration time step of 0.25 fs was used throughout all MD simulations performed in this study. More details of ReaxFF reactive potential for C/H/O/Si description and MD nanoscratch simulation can be found in Supporting Information.

3. Results and discussion

3.1. Spectral interpretation of nano-IR data

Fig. 1a and 1b show the optical image of nanoscratch lines on a silica surface and an atomic force microscopy (AFM) probe used for s-SNOM detection and the topographic image of a ~160 nm deep nanoscratch line, respectively. Fig. 1c and 1d display the second-harmonic near-field amplitude (S_2) and phase (φ_2) spectra of the scattered IR signals detected at seven locations (Figure S1 in the Supporting Information). In the spectra of the scattered IR amplitude (S_2), the main peak is observed at ~1120 cm^{-1} outside the

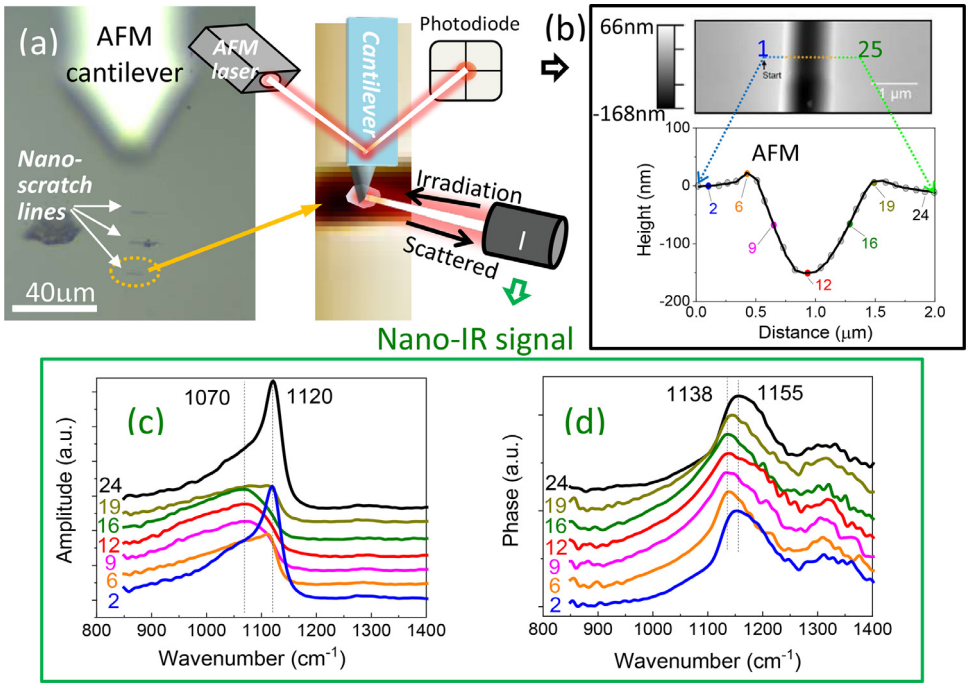

Fig. 1. (a) Optical image of AFM cantilever and nanoscratch lines and schematic illustration of nano-IR measurement. (b) AFM topography images and cross-section line profile of a nanoscratch on the silica glass surface. The nanoscratch was made with a cono-spherical tip at a constant load of 7 mN. The nano-FTIR signals were measured at 25 locations (separated by 80 nm) across the scratch line marked in the image. (c) Amplitude, S_2, and (d) phase, φ_2, data of nano-FTIR signals at selected locations. All 25 amplitude spectra can be found in Figure S1 in Supporting Information. The IR band in this region is typically attributed to the Si–O stretch mode of the glass network in the vibrational spectroscopy literature [40], but the back-scattered signal cannot be compared directly with the absorption band in IR spectroscopy (see the specular-reflection IR spectra in Figure S1a). For spectral interpretation, it must be converted to the quantity relevant to absorbance. Using the effective polarizability of the tip-sample and simple model approximations [41], the S_2 amplitude and φ_2 phase spectra of the nano-FTIR data (Fig. 1c and 1d) can be converted to the dielectric function ($\varepsilon_1 + i\varepsilon_2$) of the surface region under the tip, which then can be converted to the complex refractive index ($n + ik$); details of this conversion are given in the Supporting Information. The imaginary part (k) of refractive index is directly related to the absorptivity of the sample ($\alpha = 4\pi k/\lambda$ where λ is the wavelength of IR).

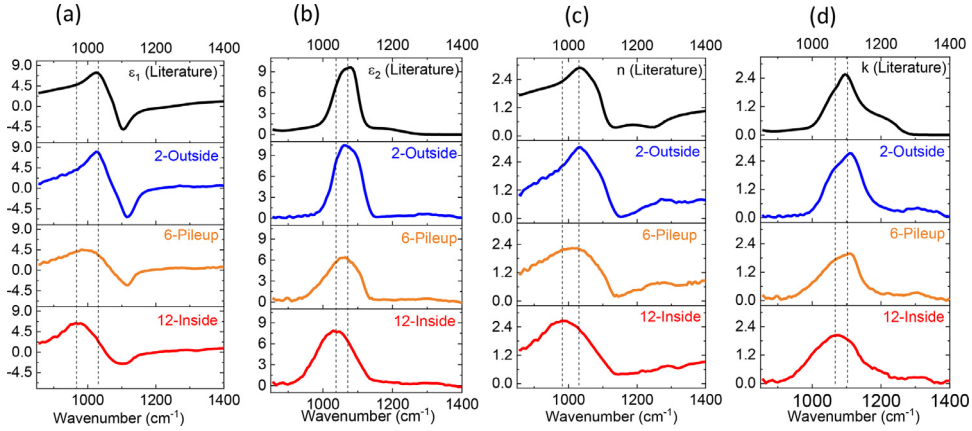

Fig. 2. Comparison of (a) real, ε_1, and (b) imaginary, ε_2, parts of dielectric function, $\varepsilon_1+i\varepsilon_2$, and (c) real, n, and (d) imaginary, k, parts of refractive index, $n+ik$, calculated from the measured amplitude (S_2) and phase (φ_2) of the nano-FTIR signals at the pristine surface (outside) versus the edge (pile-up) and vertex (inside) of the nanoscratch track. For comparison, the literature values of silica are also shown at the top.

nanoscratch line and shifted to ~1070 cm^{-1} in the nanoscratch region. This band is relatively sharp on the pristine surface and becomes weaker and broader inside the nanoscratch in the S_2 amplitude spectrum.

Fig. 2 displays the calculated dielectric function and refractive index of the pristine surface outside the nanoscratch line (position #2 in Figure S1b) and the edge (position #6) and vertex (position #12) regions of the nanoscratch line; for comparison, the reference values of silica taken from the literature are also shown [38]. The spectral shape in the calculated dielectric function of the pristine region is quite comparable with the literature, supporting that the data conversion is acceptable. Note that due to the non-equilibrium nature, the refractive index of glass can vary depending on the sample history even if the composition is the same [42]. In the s-SNOM experiment, a non-linear phase baseline drift can occur [43] and the correction for such drifting is not perfect (Figure S2). Also, the AFM tip is modeled as a sphere (Eq. S1), which is probably over-simplification. These errors propagate in the calculation (Eq. S5) converting the measured amplitude and phase (S2 and φ_2) to the complex dielectric constant. Even so, it can be clearly seen that the peak positions of the real (ε_1) and imaginary (ε_2) parts of dielectric function are significantly red-shifted to the lower

wavenumber side as the AFM probe position moves from the outside, to the pile-up edge region, and to the vertex region of the nanoscratch.

The same trend can be seen in the *n*- and *k*-spectra calculated from the dielectric function. Although the detailed shape is slightly different around 1200 cm^{-1}, the overall shape and maximum peak position in the *k*-spectrum are in agreement with the Si–O stretch band of the pristine silica glass. The main Si–O stretch band centered at 1100 cm^{-1} is shifted to ~1050 cm^{-1} and becomes broader as the position is moved from the outside to the inside of the nanoscratch.

In the vibrational spectroscopy literature of silica, the shift in the Si–O stretch mode at 1050-1200 cm^{-1} was often attributed to the change in the Si–O–Si bond angle based on the non-central force constant assumption [44,45]. However, advanced MD simulation studies on silica and sodium silicate glasses have shown that the Si–O stretch band position does not correlate consistently with the changes in the Si–O–Si angle distribution (Figure S3b); instead, it correlates linearly with the Si–O bond length change (Figure S3a) [37,38,46]. Because the force constant of the Si–O stretch mode is so large [38], a small increase in the Si–O length by 0.01 Å can be manifested as a substantial red-shift of the Si–O stretch band by ~40 cm^{-1} (Figure S3a). And the density of silica is found to have a negative correlation with the Si–O–Si bond angle (Figure S3c and S4). These recent findings collectively indicate that the densification of the silica network occurs through the decrease in the Si–O–Si bond angle and is accompanied with a small increase in the Si–O bond length.

This is consistent with previous literatures reporting the correlation between the bond parameters of silica glass and its density change under hydrostatic pressure [26–36]. Upon compression-induced densification, the Si–O–Si angle distribution shifts noticeably to a lower angle and the Si–O length increases slightly [26,28,32–34]. The O–Si–O tetrahedral angle does not change with the applied pressure [34]. The degree of densification is largely determined by the large decrease in the Si–O–Si angle (Figure S3c), which will decrease the distance between two adjacent Si atoms (Figure S4b) [32,47]. The Si–O–Si bending mode has a force constant about two orders of magnitude smaller than the Si–O stretch mode [48]; thus, the Si–O–Si angle is easier to deform to accommodate the volume change.

It should be noted that, because the glass is a non-equilibrium material, its structure has a dependence on thermal and mechanical history (Figure S3b) [37]. To verify if the correlation between bond parameter and densification found from previous studies [26,28,32–34] is applicable to the nanoscratch region, we carried out MD simulations of the subsurface damage and deformation of silica during and after the scratch with a diamond tip using ReaxFF force fields [7]. In the MD simulation (Fig. 3a), the subsurface region with large displacements is found to be densified by 7.5%. The Si–O length (Fig. 3b) and Si–O–Si angle (Fig. 3c) distributions clearly show that the nanoscratch-induced densification is accompanied with an elongation of the Si–O bond length and a noticeable decrease in the Si–O–Si bond angle. This supports that the red-shift in the S_2-spectrum (Fig. 1c) and *k*-spectrum (Fig. 2d) of the nanoscratched region is the evidence for the elongation of the Si–O bond length (Fig. 3b) [7,37,38,46]. The local molar volume change associated with the densification is due to the decrease in the Si–O-Si bond angle (Fig. 3c).

It is known that the subsurface densification induced by indentation or friction can be reverted through annealing at a temperature slightly lower than glass temperature (T_g), for example, at 0.9 × T_g (K) [7,13]. Indeed, the ReaxFF-MD simulation shows that the annealing of the nanoscratched silica glass at 1500 K for 1 ns induces shortening of the elongated Si–O length and increasing of the Si–O–Si angle toward the original values (Fig. 3b and 3c). This suggests that, upon annealing of the nanoscratched sample, the peak position in the S_2-amplitude spectrum should increase (due to shortening of the elongated Si–O bonds) and the scratch volume is recovered (due to increasing of the narrowed Si–O–Si angles). This was experimentally confirmed by re-analyzing the nanoscratch line with nano-IR after sub-T_g annealing (Figure S5).

3.2. Spectral imaging of subsurface structural changes after nanoscratch and nanoindentation

The high spatial resolution of s-SNOM-based nano-IR imaging [21,22] allows the spectral analysis to probe subsurface structural changes in and around the nano-scale mechanical deformation region. To investigate the effect of applied load, a nanoscratch line was made on the silica surface with increasing applied load. Fig. 4 compares the topography and S_2-amplitude maps at 980 cm^{-1}, 1070 cm^{-1}, and 1120 cm^{-1} of the nanoscratch before and after sub-T_g annealing. The intensity map at 1170 cm^{-1} (non-absorbing region) confirms no topographic artifacts in nano-IR detection.

When the scratch load is <0.6 mN, the residual depth is zero, suggesting that the deformation is *topography-wise fully elastic*. However, the cross-section line profile at 0.5 mN region (A in Fig. 4c) shows that the S_2-amplitude at 1120 cm^{-1} is slightly lower inside the contact area, compared to the outside. The decrease in the 1120 cm^{-1} S_2-amplitude becomes larger with the applied load in this topographically-elastic region (Figure S7a). This means that *the elongation of the Si–O bond length occurs in the subsurface region even after the elastic deformation.* Because the topographic depression is negligible, the change in the Si–O–Si bond angle (and thus the Si–Si distance) is expected to be insignificant after the elastic recovery.

The onset of plastic deformation is observed at ~0.6 mN, which corresponds to a maximum Hertzian stress of ~8 GPa. The exact yield strength of the silica glass under the given stress condition is not known. But, based on the general relationship between strength and hardness [49–51], the yield strength of silica glasses can be estimated to be around 3 GPa. During the ramp-load nanoscratch, the tip is constantly moving and thus the critical load for the onset of plastic deformation is likely to be higher than the value measured in the static condition. Considering these factors, the onset of plastic deformation at ~0.6 mN is reasonable.

When the applied load increases above 0.6 mN, the plastic deformation of glass surface is clearly seen in the topography image (Fig. 4a).The volume recovery upon sub-T_g annealing (Fig. 4b) confirms that this deformation is accompanied with the subsurface densification. Upon sub-T_g annealing, the residual depth at the maximum load decreases and a large pile-up appears around the nanoscratch edge due to the volume recovery of the densified subsurface region (Figure S7b). The decrease in the 1120 cm^{-1} S_2-amplitude appears to be linear with the residual depth (i.e., degree of densification) up to ~1.6 mN (near B in Fig. 4a) and then levels off although the residual depth keeps increasing. As the applied load continues increasing, the 1070 cm^{-1} S_2-amplitude decreases further and the 980 cm^{-1} S_2-amplitue increases (C in Fig. 4c; Figure S7a), indicating further downward shift of the Si–O stretch band as the densification continues increasing with the load. After sub-T_g annealing for 3 hours, all strained Si–O bonds are fully recovered to the original length distribution (Fig. 4b).

In the forward direction of the nanoscratch line (D in Fig. 4c; Figure S7a), the 1070 cm^{-1} and 1120 cm^{-1} S_2-amplitudes are found to be slightly lower than the outside region. This is an artifact made by the frictional slip when a secondary slip of the tip occurrs during unloading process (Figure S8a). During the unloading, the contact area between the tip and the substrate decreases, thus the shear stress applied to the surface due to the bent indenter tip increases gradually. When this stress becomes larger than the

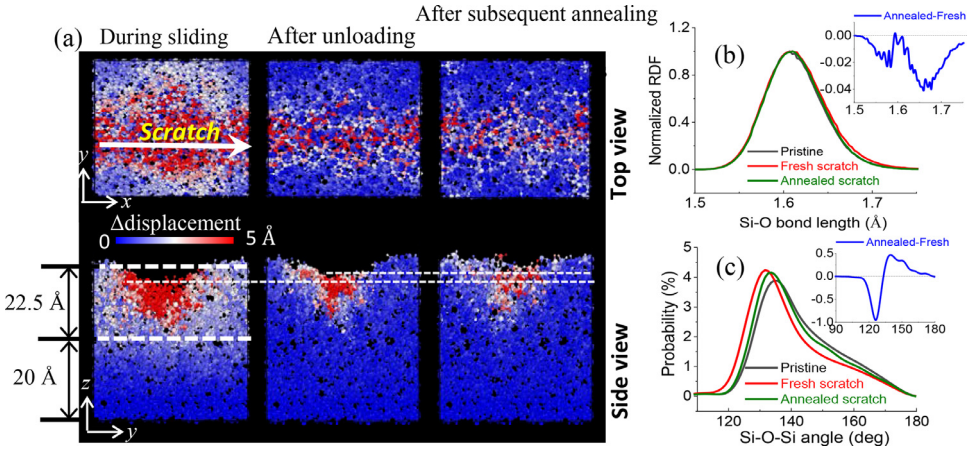

Fig. 3. (a) Snapshots from MD simulations for the nanoscratch-induced subsurface deformation at the full loading with a diamond tip at a 10 GPa contact pressure at 300 K, after unloading, and then after annealing at near glass transition temperature (T_g). The simulated silica glass is 4.16 nm × 4.22 nm × 4.52 nm; the diamond tip is not shown in the 'during sliding' image. The displacement, shown in the color scale, is from the original position before indentation and scratch with the diamond tip. (b) Normalized Si–O bond length distribution and (c) Si–O–Si bond angle distribution of the subsurface region (22.5 Å-thickness from the surface) of the silica glass upon nanoscratch and subsequent annealing. Note that, in (b) the black and green lines are overlapping. (For interpretation of the references to color in this figure legend, the reader is referred to the web version of this article.)

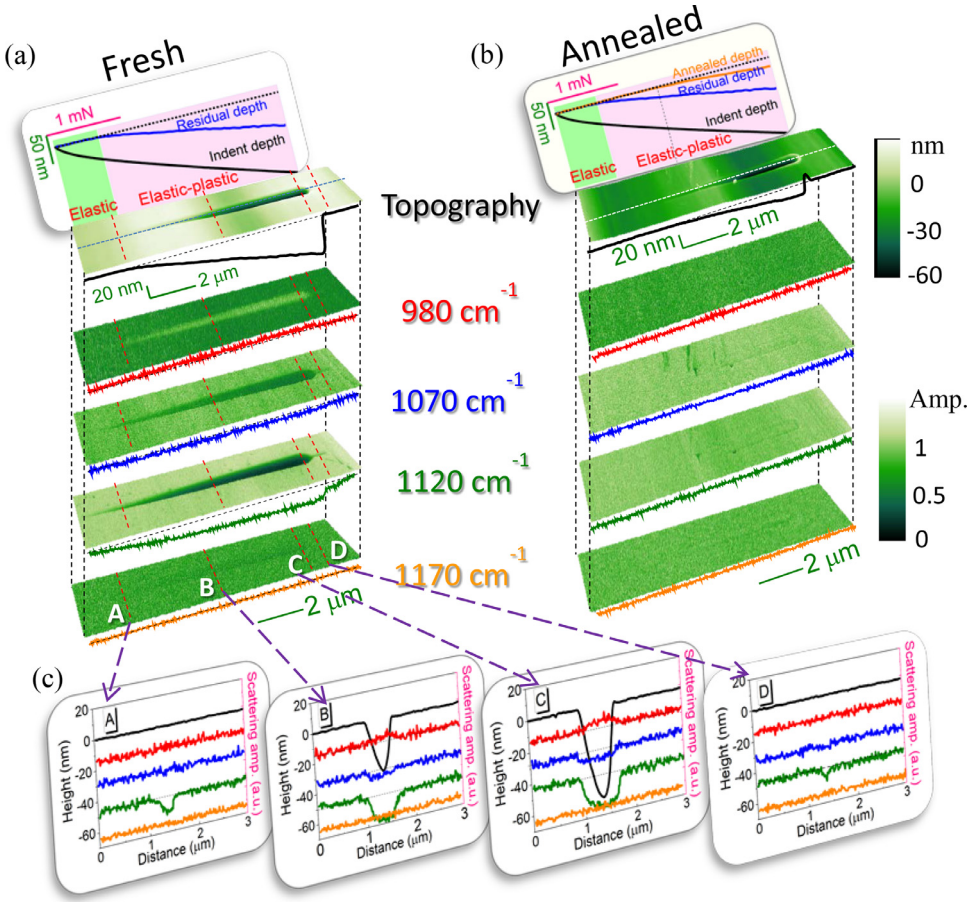

Fig. 4. AFM Topography and S_2-amplitude images of (a) fresh and (b) annealed nanoscratch on silica glass. The nanoscratch was made with a cono-spherical tip while ramping the load from zero to 3 mN at a constant rate. The penetration depth of the tip into the glass substrate during the ramp-load nanoscratch test and the residual scratch depth after removal of the tip are also shown at the top; the region marked with light green background is the elastic contact region. The topography and S_2 images are 12 μm × 3 μm in x-y directions; the S_2 image has 600 × 200 pixels. (c) Comparison of cross-section line profiles of the topography and S_2 images of the fresh nanoscratch at the positions marked in (a). The applied loads at the positions marked as A, B, and C are 0.5 mN, and 1.8 mN, and 2.8 mN, respectively. The position D is in front of the leading edge of the nanoscratch, which is the region contacted due to the secondary slip of the cono-spherical tip during the unloading process (Figure S8a). The line profiles along the scratch direction are shown in Figure S7.

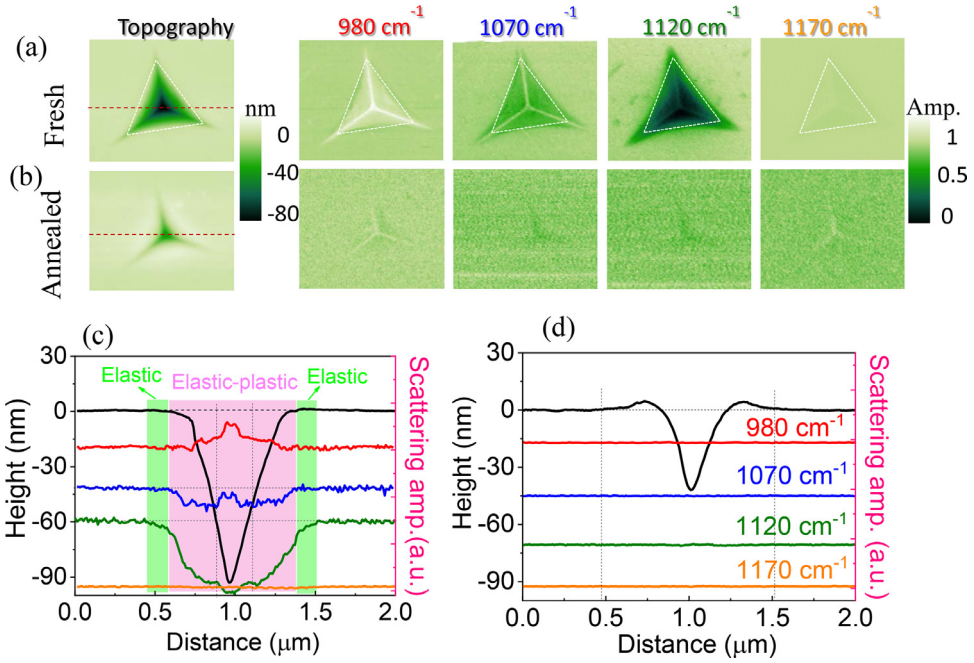

Fig. 5. (a) Topography and s-SNOM S_2 amplitude images of (a) fresh and (b) annealed nanoindentation mark on silica glass. The nanoindentation was done with a Berkovich tip at an applied load of 5 mN. The topography and S_2 images are 2 μm × 2 μm in *x-y* directions; the S_2 image has 200 × 200 pixels. The dotted white lines are added as a guide for eyes showing the three facet edges of the nanoindentation mark identified in the topography image. The plots in (c) and (d) compare the cross-section line profiles of the topography and S_2 images of the fresh and annealed nanoindentation marks, respectively, at the location marked with red lines in (a). (For interpretation of the references to color in this figure legend, the reader is referred to the web version of this article.)

shear strength of the contact, then the secondary slip of the tip in the forward direction of the scratch can occur. The fact there is no depression in the surface topography indicates that the normal load at the moment of the secondary slip is in the elastic contact regime (<0.6 mN).

Fig. 5 shows the topography and S_2-amplitude maps of the nanoindentation mark on silica produced with a Berkovich tip before and after sub-T_g annealing. Similar to the nanoscratch damage made with the cono-spherical tip (Fig. 4), the 1120 cm^{-1} S_2-amplitude is significantly reduced inside the nanoindentation mark and the 980 cm^{-1} amplitude is slightly increased; again, this suggests the elongation of the Si–O bond length due to the subsurface densification (Fig. 5a and 5c). The higher intensity of the backscattered signal at the vertex is an artifact due to the geometry of the nanoindentation mark made with the Berkovich tip (Figure S9). The subsurface densification is fully reverted upon sub-T_g annealing and all strains in the Si–O bond are reduced below the detection limit (Fig. 5b and 5d).

Similar to the nanoscratch behavior, it can be seen that the 1120 cm^{-1} S_2-amplitude is lower even in the topographically-elastic region (~100 nm region marked with green color in Fig. 5c). Thus, the subsurface structural change in the topographically-elastic region is not unique to the shear contact; it occurs even in the normal indentation without lateral friction. The 1120 cm^{-1} intensity drops suddenly at the elastic-plastic boundary in the nanoindentation mark. At the onset region of plastic deformation, the residual tensile stress may change abruptly [52,53], and this may leave a footprint in the Si–O bond length distribution.

In and around nanoindentation and nanoscratch marks, the nano-IR imaging reveals that the Si–O bond length in the subsurface region is elongated even in the region that the surface topography is full recovered indicating that the contact is fully elastic. This testifies that even if the glass surface is topographically intact, there is an atomic-scale “chemical plasticity” in the subsurface glass network structure. This finding may explain why the physically-contacted glass surface is mechanically weaker and chemically more vulnerable, although it is topographically smooth and undamaged visually [7,9,10,13,28,32,35,54] .

This discovery may incur a change of the current view on relationships between the mechanical deformation of the surface and the glass network bond parameter [54,55]. Why is the length of the stiff Si–O bond increased in response to external mechanical stress while the flexible Si–O–Si bond angle does not change in the elastic contact condition? Why is the Si–O bond elongated when the Si–O–Si bond angle is reduced upon densification due to external stress [56–59]? How does the degree of Si–O elongation quantitatively correlate with the loss of mechanical strength and chemical resistance of glass? Answering these questions may require advanced computational modeling, which should be the subject of future studies.

4. Conclusion

In summary, the nanoscale infrared spectroscopy combined with scattering-type scanning near-field optical microscopy revealed the evolution of nanoscale chemical structure of silica glass by mechanical deformation. Based on the recent advancement in spectral interpretation of the Si–O stretching vibration mode of silica and by comparing with reaction-force molecular dynamics simulations, we show that the Si–O bond length distribution of the glass network is decoupled from the bond angle change and the bond can be elongated even in the subsurface densification region as well as in the elastic contact region (with complete topographic recovery). The results clearly show the change of subsurface chemical structure in absence of surface topography variation, indicating the “chemical plasticity” of silica glass upon mechanical deformation. In the plastically deformed region with subsurface densification, the Si–O bond length is found to be longer compared to the pristine region, indicating that the densification of the glass network occurs primarily through the decrease in the Si–O–Si bond angle, not the shortening of the Si–O bond length. These findings elucidate new insights into the correlation between nanoscale

structural changes and mechanical deformations of the glass material.

Declaration of Competing Interest

The authors declare that they have no known competing financial interests or personal relationships that could have appeared to influence the work reported in this paper.

Acknowledgment

This work was supported by the National Science Foundation (Grant No. DMR-1609107, 2011410). HH was supported by the National Natural Science Foundation of China (Grant No. 51605401) and Scientific Research Fund of SiChuan Provincial Education Department (17ZA0408). YTL was supported by Corning, Inc. during the period of this work.

Supplementary materials

Supplementary material associated with this article can be found, in the online version, at doi:10.1016/j.actamat.2021.116694.

References

[1] X. Yu, T.J. Marks, A. Facchetti, Metal oxides for optoelectronic applications, Nat. Mater. 15 (2016) 383–396.
[2] K. Nomura, H. Ohta, A. Takagi, T. Kamiya, M. Hirano, H. Hosono, Room-temperature fabrication of transparent flexible thin-film transistors using amorphous oxide semiconductors, Nature 432 (2004) 488–492.
[3] F. Kotz, K. Arnold, W. Bauer, D. Schild, N. Keller, K. Sachsenheimer, T.M. Nargang, C. Richter, D. Helmer, B.E. Rapp, Three-dimensional printing of transparent fused silica glass, Nature 544 (2017) 337-229.
[4] L. Wondraczek, J.C. Mauro, J. Eckert, U. Kühn, J. Horbach, J. Deubener, T. Rouxel, Towards ultrastrong glasses, Adv. Mater. 23 (2011) 4578–4586.
[5] C.R. Kurkjian, P.K. Gupta, R.K. Brow, The strength of silicate glasses: What do we know, what do we need to know? Int. J. Appl. Glass Sci. 1 (2010) 27–37.
[6] J.R. Varner, H.J. Oel, Surface defects: their origin, characterization and effects on strength, J. Non-Cryst. Solids 19 (1975) 321–333.
[7] H. He, S.H. Hahn, J. Yu, Q. Qiao, A.C.T. Van Duin, S.H. Kim, Friction-induced subsurface densification of glass at contact stress far below indentation damage threshold, Acta Mater. 189 (2020) 166–173.
[8] H. He, L. Qian, C.G. Pantano, S.H. Kim, Mechanochemical wear of soda lime silica glass in humid environments, J. Am. Ceram. Soc. 97 (2014) 2061–2068.
[9] J. Luo, H. Huynh, C.G.Pantano Pantano, S.H. Kim, Hydrothermal reactions of soda lime silica glass-revealing subsurface damage and alteration of mechanical properties and chemical structure of glass surfaces, J. Non-Cryst. Solids 452 (2016) 93–101.
[10] J. Yu, H. He, Y. Zhang, H. Hu, Nanoscale mechanochemical wear of phosphate laser glass against a CeO_2 particle in humid air, Appl. Surf. Sci. 392 (2017) 523–530.
[11] O. Benzine, S. Bruns, Z. Pan, K. Durst, L. Wondraczek, Local deformation of glasses is mediated by rigidity fluctuation on nanometer scale, Adv. Sci. 5 (2018) 1800916.
[12] G. Brambilla, D.N. Payne, The ultimate strength of glass silica nanowires, Nano Lett. 9 (2009) 831–835.
[13] Y.F. Niu, K. Han, J.P. Guin, Locally enhanced dissolution rate as a probe for nanocontactinduced densification in oxide glasses, Langmuir 28 (2012) 10733–10740.
[14] C. Cailleteau, F. Angeli, F. Devreux, S. Gin, J. Jestin, P. Jollivet, O. Spalla, Insight into silicate-glass corrosion mechanisms, Nat. Mater. 7 (2008) 978–983.
[15] S.K. Lee, P.J. Eng, H. Mao, Y. Meng, M. Newville, M.Y. Hu, J. Shu, Probing of bonding changes in B_2O_3 glasses at high pressure with inelastic x-ray scattering, Nat. Mater. 4 (2005) 851–854.
[16] T. Geisler, L. Dohmen, C. Lenting, M.B.K. Fritzsche, Real-time in situ observations of reaction and transport phenomena during silicate glass corrosion by fluid-cell Raman spectroscopy, Nat. Mater. 18 (2019) 342–348.
[17] A. Llordés, G. Garcia, J. Gazquez, D.J. Milliron, Tunable near-infrared and visible-light transmittance in nanocrystal-in-glass composites, Nature 500 (2013) 323–326.
[18] A.J. Huber, A. Ziegler, T. Kock, R. Hillenbrand, Infrared nanoscopy of strained semiconductors, Nat. Nanotechnol. 4 (2009) 153–157.
[19] M. Liu, A.J. Sternbach, M. Wagner, T.V. Slusar, T. Kong, S.L. Bud'ko, S. Kittiwatanakul, M.M. Qazilbash, A. Mcleod, Z. Fei, E. Abreu, J. Zhang, M. Goldflam, S. Dai, G. Ni, J. Lu, H.A. Bechtel, M.C. Martin, M.B. Raschke, R.D. Averitt, S.A. Wolf, H. Kim, P.C. Canfield, D.N. Basov, Phase transition in bulk single crystals and thin films of VO_2 by nanoscale infrared spectroscopy and imaging, Phys. Rev. B 91 (2015) 245155.
[20] B. Lyu, H. Li, L. Jiang, W. Shan, C. Hu, A. Deng, Z. Ying, L. Wang, Y. Zhang, H.A. Bechtel, M.C. Martin, T. Taniguchi, K. Watanabe, W. Luo, F. Wang, Z. Shi, Phonon polariton-assisted infrared nanoimaging of local strain in hexagonal boron nitride, Nano Lett. 19 (2019) 1982–1989.
[21] L. Xiao, Z.D. Schultz, Spectroscopic imaging at the nanoscale: technologies and recent applications, Anal. Chem. 90 (2018) 440–458.
[22] G. Dominguez, A.S. Mcleod, Z. Gainsforth, P. Kelly, H.A. Bechtel, F. Keilmann, A. Westphal, M. Thiemens, D.N. Basov, Nanoscale infrared spectroscopy as a non-destructive probe of extraterrestrial samples, Nat. Commun. 5 (2014) 5445.
[23] B. Pollard, E. Muller, K. Hinrichs, M.B. Raschke, Vibrational nano-spectroscopic imaging correlating structure with intermolecular coupling and dynamics, Nat. Commun. 5 (2014) 3587.
[24] W.C. Oliver, G.M. Pharr, An improved technique for determining hardness and elastic modulus using load and displacement sensing indentation experiments, J. Mater. Res. 7 (1992) 1564–1583.
[25] E. Moayedi, L. Wondraczek, Quantitative analysis of scratch-induced microabrasion on silica glass, J. Non-Cryst. Solids 470 (2017) 138–144.
[26] N.M. Trease, T.M. Clark, P.J. Grandinetti, J.F. Stebbins, S. Sen, Bond length-bond angle correlation in densified silica -results from ^{17}O NMR spectroscopy, J. Chem. Phys. 146 (2017) 184505.
[27] Y. Liang, C.R. Miranda, S. Scandolo, Temperature-induced densification of compressed SiO_2 glass: a molecular dynamics study, High Pressure Res 28 (2008) 35–44.
[28] C.J. Benmore, E. Soignard, S.A. Amin, M. Guthrie, S.D. Shastri, P.L. Lee, J.L. Yarger, Structural and topological changes in silica glass at pressure, Phys. Rev. B 81 (2010) 054105.
[29] Y. Shimada, M. Okuno, Y. Syono, M. Kikuchi, K. Fukuoka, N. Ishizawa, An X-ray diffraction study of shock-wave-densified SiO_2 glasses, Phys. Chem. Min. 29 (2002) 233–239.
[30] L. Huang, J. Kieffer, Amorphous-amorphous transitions in silica glass. I. reversible transitions and thermomechanical anomalies, Phy. Rev. B. 69 (2004) 224203.
[31] T. Deschamps, C. Martinet, J.L. Bruneel, B. Champagnon, Soda-lime silicate glass under hydrostatic pressure and indentation: a micro-Raman study, J. Phys. 23 (2011) 035402.
[32] D. Wakabayashi, N. Funamori, T. Sato, Enhanced plasticity of silica glass at high pressure, Phys. Rev. B 91 (2015) 014106.
[33] C. Meade, R.J. Hemley, H.K. Mao, High-pressure x-ray diffraction of SiO_2 glass, Phys. Rev. Lett. 69 (1992) 1387.
[34] R.G. Della Valle, E. Venuti, High-pressure densification of silica glass: a molecular-dynamics simulation, Phys. Rev. B 54 (1996) 3809.
[35] N. Li, R. Sakidja, S. Aryala, W. Ching, Densification of a continuous random network model of amorphous SiO_2 Glass, Phys. Chem. Chem. Phys. 16 (2014) 1500–1514.
[36] B.T. Poe, C. Romano, G. Henderson, Raman and XANES spectroscopy of permanently densified vitreous silica, J. Non-Cryst. Solids 341 (2004) 162–169.
[37] J. Luo, Y. Zhou, C.G. Pantano, S.H. Kim, Correlation between IR peak position and bond parameter of silica glass: molecular dynamics study on fictive temperature (cooling rate) effect, J. Am. Ceram. Soc. 101 (2018) 5419–5427.
[38] J. Luo, Y. Zhou, S.T. Milner, C.G. Pantano, S.H. Kim, Molecular dynamics study of correlations between IR peak position and bond parameters of silica and silicate glasses: effects of temperature and stress, J. Am. Ceram. Soc. 101 (2018) 178–188.
[39] S. Plimpton, Fast parallel algorithms for short-range molecular dynamics, J. Comput. Phys. 117 (1995) 1–19.
[40] A. Agarwal, M. Tomozawa, Correlation of silica glass properties with the infrared spectra, J. Non-Cryst. Solids 209 (1997) 166–174.
[41] F. Keilmann, R. Hillenbrand, Near-field microscopy by elastic light scattering from a tip, Phil. Trans. R. Soc. Lond. A 362 (2004) 787–805.
[42] R. Kitamura, L. Pilon, M. Jonasz, Optical constants of silica glass from extreme ultraviolet to far infrared at near room temperature, Appl. Optics. 46 (2007) 8118–8133.
[43] I. Amenabar, S. Poly, M. Goikoetxea, W. Nuansing, P. Lasch, R. Hillenbrand, Hyperspectral infrared nanoimaging of organic samples based on Fourier transform infrared nanospectroscopy, Nat. Commun 8 (2017) 14402.
[44] F.L. Galeener, Band limits and the vibrational spectra of tetrahedral glasses, Phys. Rev. B. 19 (1979) 4292–4297.
[45] K. Ishikawa, K. Suzuki, S. Okamura, Asymmetric peak line shape of infrared dielectric function spectra for thermally grown silicon dioxide films, J. Appl. Phys. 88 (2000) 7150.
[46] H. Liu, S.H. Hahn, M. Ren, M. Thiruvillamalai, T.M. Gross, J. Du, A.C.T. Van Duin, S.H. Kim, Searching for correlations between vibrational spectral features and structural parameters of silicate glass network, J. Am. Ceram. Soc. 103 (2020) 3575–3589.
[47] R.L. Mozzi, B.E. Warren, The structure of vitreous silica, J. Appl. Cryst. 2 (1969) 164–172.
[48] R.A.B. Devine, Ion implantation- and radiation-induced structural modifications in morphous SiO_2, J. Non- Cryst. Solids. 152 (1993) 50–58.
[49] P. Zhang, S.X. Li, Z.F. Zhang, General relationship between strength and hardness, Mater. Sci. Eng. A 529 (2011) 62–73.
[50] Z. Chen, X. Wang, A. Atkinson, N. Brandon, Spherical indentation of porous ceramics: elasticity and hardness, J. Eur. Ceram. Soc. 36 (2016) 1435–1445.
[51] T. Fischer, H. Tomizawa, Interaction of tribochemistry and microfracture in the friction and wear of silicon nitride, Wear 105 (1985) 29–45.

[52] S. Bensmann, F. Gaußmann, M. Lewin, J. Wüppen, S. Nyga, C. Janzen, B. Jungbluth, T. Taubner, Near-field imaging and spectroscopy of locally strained GaN using an IR broadband laser, Opt. Exp. 22 (2014) 22369–22381.
[53] K. Asai, S. Yoshida, A. Yamada, J. Matsuoka, A. Errapart, C.R. Kurkjian, Micro-photoelastic evaluation of indentation-induced stress in glass, Mater. Trans. 60 (2019) 1423–1427.
[54] E.C. Ziemath, P.S.P. Herrmann, Densification and residual stresses induced in glass surfaces by Vickers indentations, J. Non-Cryst. Solids 273 (2000) 19–24.
[55] A. Winterstein-Beckmanna, D. Mönckea, D. Pallesb, E.I. Kamitsosb, L. Wondraczek, A Raman-spectroscopic study of indentation-induced structural changes in technical alkali-borosilicate glasses with varying silicate network connectivity, J. Non-Cryst. Solids 405 (2014) 196–206.
[56] R.A.B. Devine, J. Arndt, Si-O bond-length modification in pressure-densified amorphous, Phys. Rev. B 35 (1987) 9376–9379.
[57] C. Calahoo, J.W. Zwanziger, I.S. Butler, Mechanical-structural investigation of ion-exchanged lithium silicate glass using micro-Raman spectroscopy, J. Phys. Chem. C 120 (2016) 7213–7232.
[58] M.T. Lan, T.T. Duong, T. Iitaka, N.V. Hong, Computer simulation of $CaSiO_3$ glass under compression: correlation between Si-Si Pair radial distribution function and intermediate range order structure, Mater. Res. Exp. 4 (2017) 065201.
[59] M.G. Tucker, M.T. Dove, D.A. Keen, Simultaneous analysis of changes in long-range and short-range structural order at the displacive phase transition in quartz, J. Phys. 12 (2000) L723–L730.